

Fluorescent Benzoxazine–Perylene Linked Covalent Organic Polymer as a Sensing Probe for Lead Ions and 2,4,6-Trinitrophenol

Mohsin Ejaz, Mohamed Gamal Mohamed, and Shiao-Wei Kuo*

Cite This: *ACS Appl. Polym. Mater.* 2024, 6, 9170–9179

Read Online

ACCESS |



Metrics & More



Article Recommendations

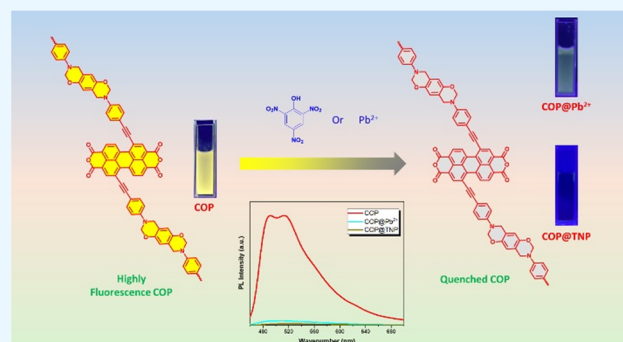


Supporting Information

ABSTRACT: This research explores fluorescent covalent organic polymer (COP) as light-emitting materials due to their porous nature and π -conjugated skeleton. We successfully synthesized a fluorescent COP, named Pery-DHTP-BZ-COP, using the Sonogashira–Hagihara coupling reaction. This reaction combines 3,8-bis(4-ethynylphenyl)-2,3,4,7,8,9-hexahydrobenzo[1,2-*e*:4,5-*e'*]bis([1,3]-oxazine) (DHTP-BZ) with 1,7-dibromoperylene dianhydride (Pery-Br₂). We confirmed the existence of the benzoxazine (BZ) ring and the overall structure of Pery-DHTP-BZ-COP using FTIR and NMR spectroscopy. The FTIR, DSC, and TGA analyses were employed to investigate the thermal ring-opening polymerization (ROP) behavior and thermal stability of Pery-DHTP-BZ-COP at various temperatures. Photoluminescence (PL) spectroscopy and ultraviolet (UV) light were used to demonstrate the fluorescence emission properties of Pery-DHTP-BZ-COP dispersed in a solution. These

fluorescent properties, combined with the electron-rich nature of the COP, led us to develop a sensor for selective and accurate detection of lead ions (Pb²⁺) and a nitroaromatic explosive, trinitrophenol (TNP). The electron-rich nature of Pery-DHTP-BZ-COP facilitates efficient electron transfer to the target analytes (Pb²⁺ and TNP). This electron transfer process results in the fluorescence quenching of the COP, allowing for detection. The sensor exhibits a desirable linear response to both Pb²⁺ and TNP with remarkably low detection limits of 0.5 μ M (0.163 ppm) and 0.7 μ M (0.16 ppm), respectively.

KEYWORDS: benzoxazine, covalent organic polymer, fluorescence, Sonogashira–Hagihara coupling, lead ions, trinitrophenol



INTRODUCTION

Heavy metal ions and explosive nitroaromatics are becoming more and more of a problem due to the fast expansion of agriculture and industry. These pollutants inflict permanent damage to aquatic life and human health.^{1–5} Heavy metals refer to a collection of metals and metalloids that possess a relatively high density and are poisonous, even at parts per billion (ppb) concentrations.^{6–8} The predominant heavy metal contaminants found in wastewater include cadmium, chromium, copper, lead, mercury, nickel, silver, and zinc.⁹ The enduring presence of these substances is attributed to their non-biodegradable and poisonous properties, rendering them a substantial threat to the well-being of animals and people who rely on water as an essential need for survival.¹⁰ Furthermore, these substances have the potential to accumulate in soil and water, ultimately entering the food chain and leading to enduring health issues, including kidney failure, neurological diseases, and cancers.¹¹ Among different metal ions, lead (Pb²⁺) is a frequently used material in several economic sectors, including agriculture, medicines, and industries like batteries, pigments, and metallurgy.^{12,13} Pb²⁺ has been classified by the World Health Organization (WHO) as one of the most hazardous elements for the environment, human

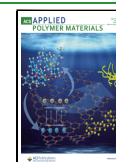
health, and animals.¹⁴ Even a tiny concentration of Pb²⁺ ions may significantly impairments in brain function and result in neurological breakdown.¹⁵ Therefore, detecting Pb²⁺ metal ions is important due to their toxicity. Nitroaromatic compounds, which are used as chemical weapons, present a significant risk to the safety of both civilians and the military.^{16,17} Additionally, they are understood as hazardous pollutants that contribute to environmental contamination. These materials commonly used are nitro-substituted compounds, such as 2,4,6-trinitrophenol (TNP), 2,4-dinitrotoluene (DNT), and 2,4,6-trinitrotoluene (TNT). These materials consist of a strong combination of a chemical oxidant and a reluctant substance, which endures a highly exothermic decomposition process, leading to significant environmental pollutants.¹⁸ Furthermore, TNP is considered one of the strongest organic acids due to its composition of strong

Received: May 16, 2024

Revised: July 4, 2024

Accepted: July 8, 2024

Published: July 22, 2024



electron-withdrawing groups. In comparison to TNT, TNP exhibits higher explosive potential.^{19–21} Furthermore, its widespread application in the pharmaceutical, dye, and leather sectors, as well as in the production of matches, fireworks, and rocket propellant, has inevitably resulted in soil and ground-water contamination.^{22–24} The TNP has been classified as an active carcinogen by the Environmental Protection Agency (EPA), which has issued warnings regarding the detrimental health effects it can cause with protracted exposure.^{25,26} The consumption of these dangerous compounds has resulted in the growth of environmental pollutants, ultimately causing soil and water contamination.^{27–29} Hence, it is essential to streamline the development of a sensor probe capable of detecting heavy metal ions and explosive nitroaromatic compounds. Porous organic polymers (POPs) consist of lightweight elements, such as carbon, hydrogen, oxygen, nitrogen, and boron. They have been consistently growing as a highly potential category of porous materials in recent times compared to typical inorganic porous materials like zeolite and activated carbon.^{30–34} POPs have many benefits, including lowered skeletal density, a greater specific surface area, and excellent physicochemical stability. The abundance of organic building blocks enables the diversity and adaptability of POPs for various applications, such as adsorption,³⁵ separation,³⁶ gas storage,^{37,38} energy conversion,³⁹ drug delivery,⁴⁰ heterogeneous catalysis,^{41,42} and sensing.⁴³ In the past few years, different types of POPs have been developed, including covalent–organic frameworks (COFs),⁴⁴ conjugated microporous polymers (CMPs),⁴⁵ and covalent organic polymers (COPs).⁴⁶ These materials have been used as sensing platforms because they possess the following advantageous qualities, e.g., controlled polymer structure, π -conjugated, designable building blocks, sensing moieties, luminescence properties, and high stability in acid or base. The inherent advantages of POPs make them highly suitable for chemical sensing applications.^{47–49} Benzoxazines (BZs) are intriguing heterocyclic compounds that are synthesized by the typical condensation reactions of paraformaldehyde, primary aromatic or aliphatic amines, and aromatic phenolic derivatives. These compounds have nitrogen and oxygen atoms arranged in a six-membered oxazine ring. BZs undergo ring-opening polymerization at mild temperatures to produce highly thermally stable polybenzoxazines (PBZs).^{50–54} These have attracted a lot of attention recently due to their remarkable chemical and mechanical properties, low dielectric value constants, superior flame retardancy, and decreased surface-free energies.^{55–57} There have been several recent publications on incorporating benzoxazine into luminous chemicals and polymers.^{55,58–61} The benzoxazine monomers and polymers reported earlier have shown attractive properties, which have prompted ongoing endeavors to explore and produce new benzoxazine-based fluorescence compounds. The Hui group utilized a TPE-BOZ precursor as a probe, revealing the presence of picric acid (PA).⁶² Additionally, as reported by Shi et al., TPE-decorated PBZ exhibited an AIE property and acted as a fluorescent probe for DNP, boasting a detection limit of approximately 7.4×10^{-7} M.⁶³ Based on the facts provided above, in this work, the Sonogashira–Hagihara coupling process was employed to successfully synthesize Pery-DHTP-BZ-COP, a newly developed fluorescent material. This COP, constructed using DHTP-BZ and Pery-Br₂, showcases exceptional fluorescence and thermal stability characteristics. We explored the potential of utilizing Pery-DHTP-BZ-COP as a fluorescent probe for the

selective and sensitive detection of Pb²⁺ and the explosive TNP. The quenching of fluorescence observed in Pery-DHTP-BZ-COP upon exposure to TNP and Pb²⁺ ions is attributed to photoinduced electron transfer (PET). This mechanism enables effective fluorescence quenching and facilitates electron transfer from the Pery-DHTP-BZ-COP to the analytes, enabling their detection. This study establishes the foundation for the practical application of functional porous materials like Pery-DHTP-BZ-COP in the real-time detection of TNP and Pb²⁺ ions.

EXPERIMENTAL SECTION

Materials. *N,N*-Dimethylformamide (DMF), calcium chloride (CaCl₂), mercury(II) chloride (HgCl₂), chromium(III) chloride (CrCl₃), lead(II) acetate [Pb(C₂H₃O₂)₂], potassium dichromate (K₂Cr₂O₇), and perylene-3,4,9,10-tetracarboxylic dianhydride (Pery-Dianhydride, 97%) were purchased from Alfa Aesar. The Pd(PPh₃)₄, iron(III) chloride, copper(I) iodide (CuI), sodium chloride (NaCl), zinc chloride (ZnCl₂), ferrous chloride (FeCl₂), magnesium chloride (MgCl₂), cuprous chloride (CuCl₂), cobalt(II) chloride (CoCl₂), and triethylamine (Et₃N) were purchased from Sigma-Aldrich. The two building blocks, Pery-Br₂ and DHTP-BZ, were prepared following our previously established protocol.^{34,51}

Synthesis of Pery-DHTP-BZ-COP. Pery-DHTP-BZ-COP was synthesized via a Sonogashira–Hagihara coupling reaction. The first step involved combining Pd(PPh₃)₄ (0.044 g, 0.038 mmol), DHTP-BZ (0.15 g, 0.38 mmol), Pery-Br₂ (0.34 g, 0.38 mmol), 0.01 g (0.038 mmol) of PPh₃, and 0.007 g (0.038 mmol) of CuI in 20 mL of Et₃N/DMF (1:1) in a reaction vessel. The mixture underwent three cycles of freeze–pump–thaw degassing to remove any dissolved oxygen. Subsequently, the mixture was refluxed to 100 °C for 72 h to promote the coupling reaction. After 72 h, the reaction mixture was cooled, and the product was isolated as a brown solid. This brown solid was then thoroughly put in THF, MeOH, and acetone to remove any residual monomers and impurities. Finally, purified Pery-DHTP-BZ-COP was dried at 50 °C for 24 h.

RESULTS AND DISCUSSION

Synthesis, Characterization, and Thermal Polymerization of Pery-DHTP-BZ-COP. We successfully prepared and designed the Pery-DHTP-BZ-COP framework using a Sonogashira–Hagihara coupling reaction between Pery-Br₂ and DHTP-BZ (Figure 1a). The reaction was kept at 100 °C for 3 days with solvents (DMF and Et₃N) and a catalyst, Pd(PPh₃)₄. Detailed procedures for synthesizing the monomers DHTP-BZ and Pery-Br₂ and FTIR data of Pery-Br₂ can be found in the Supporting Information (Schemes S1 and S2 and Figure S1). FTIR, solid-state NMR, and DSC analyses were employed to validate the existence of the BZ ring within the Pery-DHTP-BZ-COP framework. Figure 1b compares the FTIR spectra of DHTP-BZ and Pery-DHTP-BZ-COP. In our previous study, the characteristic peaks in the DHTP-BZ spectrum were identified at 936, 1228, 2098, and 3222 cm⁻¹ corresponding to oxazine, C–O–C, C≡C, and ≡C–H, respectively.⁵¹ After the Sonogashira–Hagihara coupling, the ≡C–H bond (3222 cm⁻¹) disappeared completely, validating the successful cross-linking between Pery-Br₂ and DHTP-BZ. The remaining peaks observed in the FTIR spectrum of Pery-DHTP-BZ-COP at 2175, 1750, 1602, and 927 cm⁻¹ correspond to C≡C, C=O, C=C, and oxazine ring, respectively. These peaks further validate the presence of the desired BZ and Pery units within the COP structure. Solid-state ¹³C NMR spectroscopy was employed to analyze Pery-DHTP-BZ-COP due to its cross-linked nature, which renders it insoluble in common organic solvents. Figure 1c depicts the

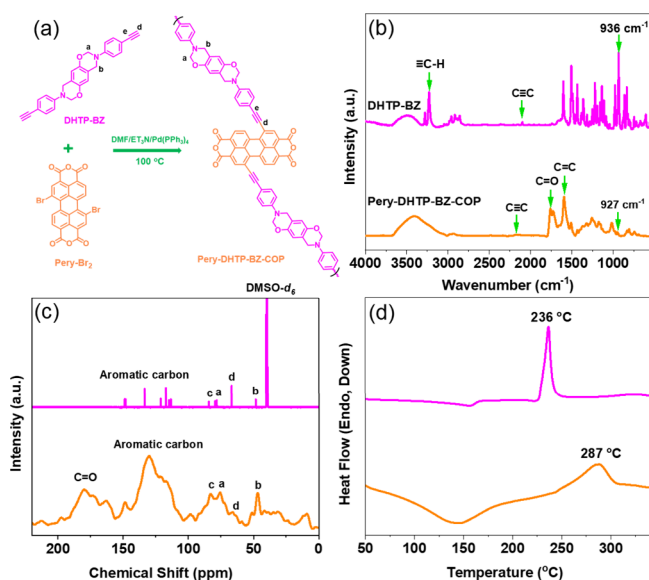


Figure 1. (a) Synthesis of Pery-DHTP-BZ-COP. (b) FTIR, (c) ^{13}C NMR, and (d) DSC spectra of DHTP-BZ and Pery-DHTP-BZ-COP.

solid-state ^{13}C NMR pattern of the COP framework alongside the solution-state ^{13}C NMR spectrum of DHTP-BZ for comparison. The COP framework spectrum exhibits peaks at 180 ppm (C=O), 110–140 ppm (aromatic carbons), 75 ppm (OCH₂N), and 46 ppm (ArCH₂N), as seen in Figure 1c. The consistency observed between the FTIR and NMR analyses confirms the successful incorporation of the BZ linkage within the Pery-DHTP-BZ-COP framework following the Sonogashira–Hagihara coupling reaction. The DSC analysis was employed to investigate the ROP behavior of Pery-DHTP-BZ-COP (Figure 1d).

The DSC curve revealed an exothermic curing temperature of Pery-DHTP-BZ-COP at 287 °C. The cross-linked structure formed during the Sonogashira–Hagihara coupling reaction hinders the ROP of the BZ ring within the COP framework. This hindered ring-opening translates to a higher thermal polymerization temperature for the COP framework compared to the DHTP-BZ monomer (236 °C).⁵⁴ We further explored the ROP and thermal stability of Pery-DHTP-BZ-COP using a combination of DSC, FTIR, and TGA analysis (Figure 2). The DSC curves for Pery-DHTP-BZ-COP at 25, 100, and 200 °C displayed curing peaks at different temperatures (287, 272, and 285 °C, respectively) alongside melting peaks (144, 165, and 143 °C, respectively). This observation suggests a partial ring-opening polymerization (ROP) process. The absence of a curing peak in the 300 °C DSC curve indicates complete ROP, resulting in poly(Pery-DHTP-BZ-COP) (Figure 2a). The FTIR spectra obtained at different temperatures support the ROP process at 300 °C. The signals corresponding to the BZ unit vanished entirely in the FTIR profile acquired at 300 °C (Figure 2b). This disappearance aligns with the complete ROP of the oxazine ring observed in the DSC analysis. TGA analysis was employed to investigate the thermal stability of Pery-DHTP-BZ-COP under various curing temperatures (Figure 2c). The Pery-DHTP-BZ-COP exhibited a thermal decomposition temperature (T_{d10}) of 261 °C and a char yield of 57 wt %. Notably, the thermal stability and char yield improved significantly after heat treatment at 300 °C. The T_{d10} increased to 404 °C, and the char yield reached 60 wt %. This remarkable improvement in thermal stability can be primarily attributed to a highly cross-linked poly(Pery-DHTP-BZ-COP) structure after complete ROP. Additionally, the extensive intra- and intermolecular hydrogen bonding (OH⋯O) established during ROP plays a crucial role in enhancing the thermal stability of the material.^{51–53} Following the ROP process, Pery-

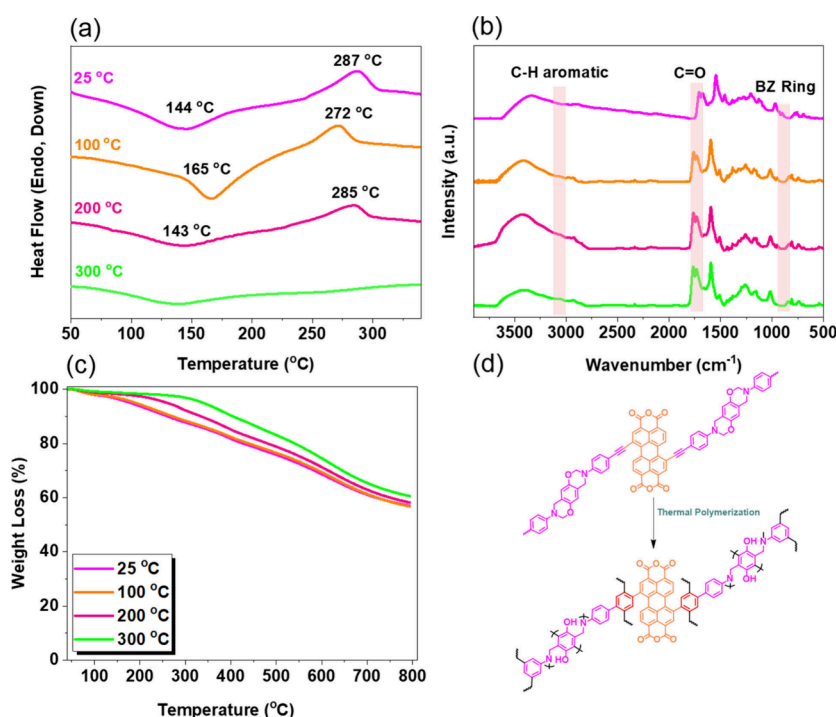


Figure 2. ROP behavior of Pery-DHTP-BZ-COP was investigated by (a) DSC, (b) FTIR, and (c) TGA, and (d) expected ROP of Pery-DHTP-BZ-COP to form a highly cross-linked poly(Pery-DHTP-BZ-COP).

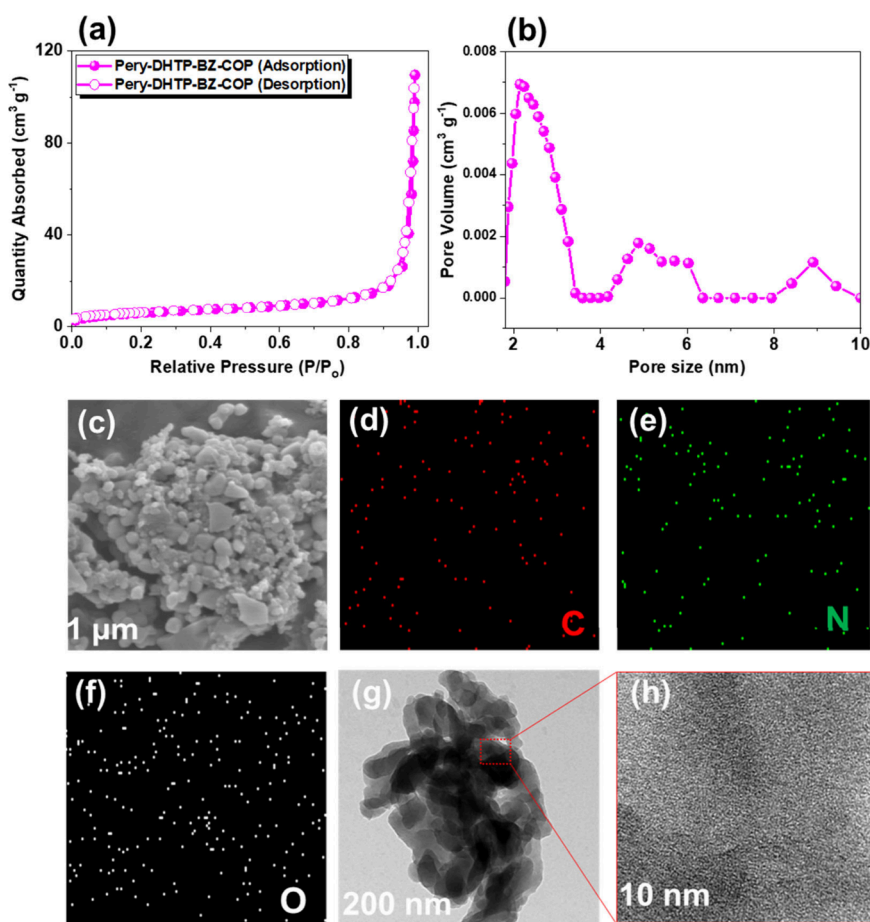


Figure 3. (a) N₂ adsorption/desorption isotherms, (b) pore size distribution profile, (c–f) SEM and SEM-EDS images with their corresponding element mapping (C, N, and O), and (g, h) TEM images of Pery-DHTP-BZ-COP.

DHTP-BZ-COP is envisioned to adopt the chemical structure depicted in Figure 2d and Scheme S3. Powder X-ray diffraction (PXRD) analysis was employed to characterize the material's nature. The resulting PXRD pattern exhibited broad peaks, a signature of amorphous materials (Figure S2). This observation suggests that Pery-DHTP-BZ-COP lacks well-defined, long-range order in its atomic arrangement.

Porosity and Morphology of Pery-DHTP-BZ-COP.

Nitrogen sorption experiments at 77 K were conducted to evaluate the porosity of Pery-DHTP-BZ-COP. The material displayed type I isotherms in the adsorption–desorption plot (Figure 3a). This characteristic behavior, with N₂ adsorption occurring primarily at high pressures ($P/P_0 > 0.1$), signifies the presence of mesoporous structures within the COP. The Brunauer–Emmett–Teller (BET) method was used to determine the specific surface area and pore volume of Pery-DHTP-BZ-COP based on the data from Figure 3a.

The analysis revealed a specific surface area of 25 m² g⁻¹ and a pore volume of 0.144 cm³ g⁻¹. Nonlocal density functional theory (NDFT) was employed to analyze the pore size distribution in Pery-DHTP-BZ-COP. Figure 3b depicts the distribution, highlighting a dominant peak at 2.18 nm and further confirming the presence of mesopores. Both SEM and TEM were used to examine the morphology of Pery-DHTP-BZ-COP. The SEM image in Figure 3c reveals aggregated spherical particles. Additionally, SEM-EDS mapping (Figure 3d–f) confirms the presence of carbon, nitrogen, and oxygen within the Pery-DHTP-BZ-COP structure. TEM analysis

(Figure 3g) corroborates the findings from SEM, demonstrating the presence of aggregated spherical particles. Furthermore, the image in Figure 3h, with its contrasting black and white regions, visually suggests the porous characteristics of Pery-DHTP-BZ-COP.

Fluorescence Properties of Pery-DHTP-BZ-COP. UV–vis absorbance analysis of the Pery-DHTP-BZ-COP in various organic solvents, including methanol, acetone, and ethanol, revealed an $n-\pi^*$ absorbance peak centered between 467.1 and 510.48 nm (Figure S3). We investigated the fluorescence properties of dispersed Pery-DHTP-BZ-COP in organic solvents using PL spectroscopy and under a UV lamp at 365 nm (Figure 4). The experiment examined how the COP's fluorescence behaved when dispersed in different organic solvents. Figure 4a displays the Pery-DHTP-BZ-COP dispersed in various organic solvents and illuminated with UV light. Interestingly, Pery-DHTP-BZ-COP exhibited distinct fluorescence colors depending on the solvent. Notably, the Pery-DHTP-BZ-COP dispersed in methanol produced the brightest yellow fluorescence, suggesting a potentially stronger emission intensity compared with other solvents. To gain further insight, PL spectra of Pery-DHTP-BZ-COP dispersed in different solvents were recorded at an excitation wavelength of 350 nm (Figure 4b). The results confirmed the visual observations. In methanol, the PL spectrum displayed a prominent emission peak at 515 nm, which was significantly higher than those observed with THF, acetone, and water. Interestingly, the ethanol and DMF solutions did not exhibit

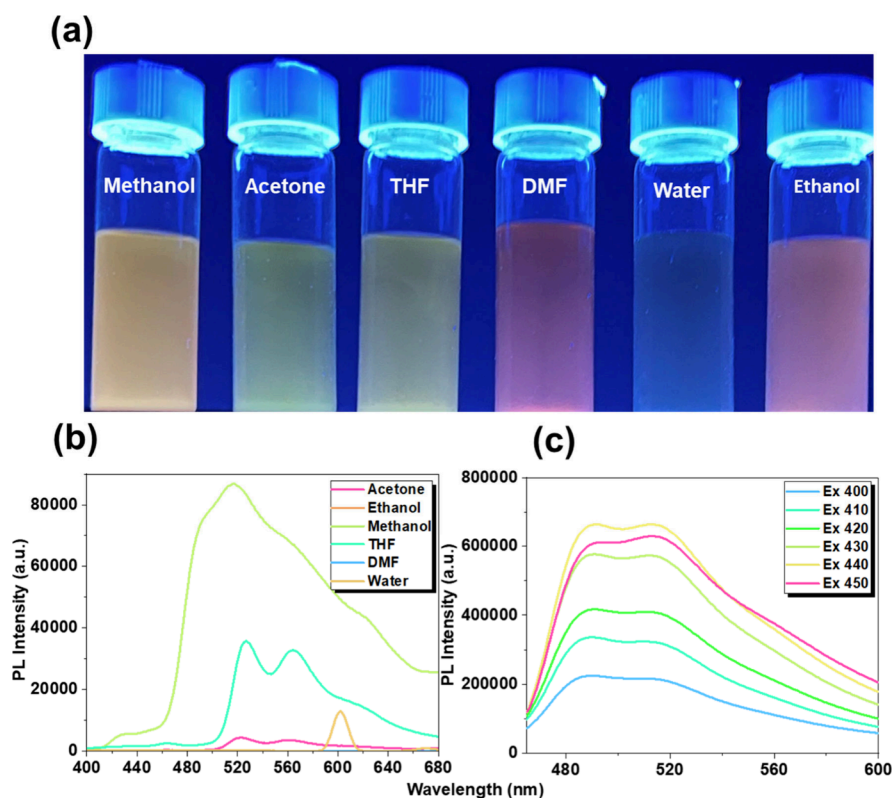


Figure 4. (a) UV image of dispersed Pery-DHTP-BZ-COP in different organic solvents. (b) PL spectra of dispersed Pery-DHTP-BZ-COP in different organic solvents (excitation: 350 nm). (c) PL spectra of methanol dispersed Pery-DHTP-BZ-COP at different excitation wavelengths.

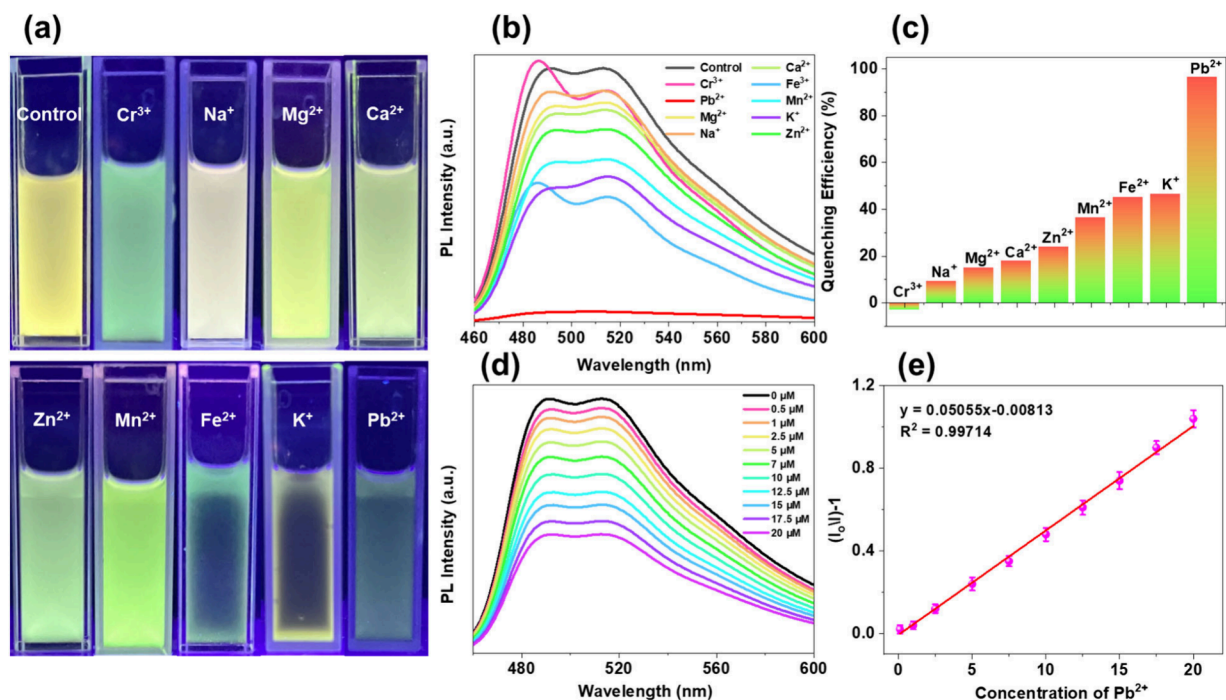


Figure 5. (a) UV images of different metal ions in the Pery-DHTP-BZ-COP, (b) their PL spectra, (c) quenching efficiencies, (d) fluorescence titration by varying concentration of Pb²⁺, and (e) linear graph corresponding to PL intensity and Pb²⁺ concentration.

any emission peaks. We focused all subsequent fluorescence studies on Pery-DHTP-BZ-COP dispersed in methanol. Several factors can influence the variation in the fluorescence color and intensity observed when a polymer interacts with different organic solvents. These factors include solvatochrom-

ism, aggregation-induced emission, and interactions between the polymer and solvents.^{64,65}

Since fluorescence emission intensity directly depends on the excitation wavelength,^{66–68} to achieve the maximum emission intensity, we recorded PL spectra at various excitation

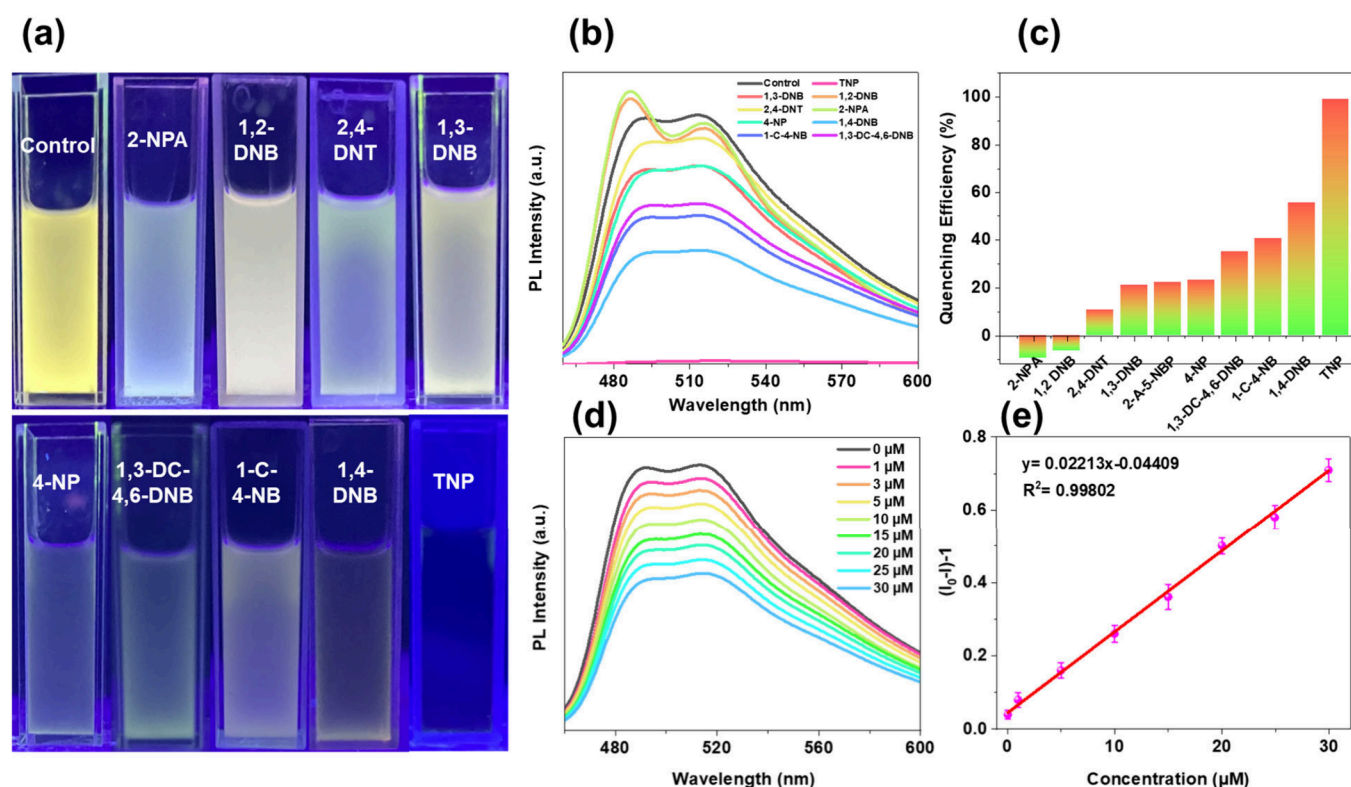


Figure 6. (a) UV images of different nitroaromatics in the Pery-DHTP-BZ-COP, (b) their PL spectra, (c) quenching efficiencies, (d) fluorescence titration by varying concentration of TNP, and (e) linear graph corresponding to PL intensity and TNP concentration.

wavelengths ranging from 400 to 450 nm (Figure 4c). The results revealed that Pery-DHTP-BZ-COP exhibited the strongest PL emission when excited at a wavelength of 440 nm. Therefore, all further investigations concerning the fluorescence properties of Pery-DHTP-BZ-COP employed this optimized excitation wavelength. To examine the impact of additional water content on the emission of Pery-DHTP-BZ-COP in a methanol solution, PL spectra were analyzed. The results showed that as the water content increased, the emission of Pery-DHTP-BZ-COP progressively decreased compared to its emission in pure methanol solution (Figure S4). These findings suggest that the Pery-DHTP-BZ-COP framework is not an AIE material. Additionally, the emission peak of the Pery-DHTP-BZ-COP framework decreased as the pH increased from 3 to 11, as shown in Figure S5.

Fluorescent Probe Pery-DHTP-BZ-COP for the Detection of Pb²⁺ Ions and TNP. Heavy metal contamination in water bodies poses a significant threat to environmental safety and human health. Driven by the excellent fluorescence properties and electron-rich framework of Pery-DHTP-BZ-COP, we explored its potential as a fluorescent sensor for detecting metal ions in aqueous environments, mimicking real-world applications. Aqueous solutions of various metal ions (Co³⁺, Cr²⁺, Pb²⁺, Mg²⁺, Na⁺, Fe²⁺, Ca²⁺, Cu²⁺, Fe³⁺, Mn²⁺, K⁺, Zn²⁺, and Hg²⁺) were prepared and sonicated for 3 h. Subsequently, we investigated the fluorescence quenching behavior of Pery-DHTP-BZ-COP dispersed in methanol upon the introduction of individual metal ion analytes. Observations were made under UV light and through PL spectra recorded at room temperature (Figure 5). Figures 5a and S6 display the effect of different metal analytes on the fluorescence of Pery-DHTP-BZ-COP under UV light. The bright yellow emission of COP exhibited a significant quenching response upon the

introduction of Pb²⁺ ions, visually confirming its detection potential. This observation was further corroborated by the PL spectra in Figure 5b, which showed a substantial decrease in fluorescence intensity for the Pb²⁺ addition compared to other metal analytes. The quenching efficiency for Pb²⁺ ions was calculated to be 96.7% using the formula provided in eq 1 of the Supporting Information, significantly higher than for any other metal analyte (Figure 5c). To quantify the sensor's sensitivity toward Pb²⁺, a fluorescence titration experiment was conducted (Figure 5d). The Pb²⁺ ion concentration was varied from 0 to 20 μM, and the fluorescence intensity displayed a linear decrease with increasing concentration. The linear correlation coefficient obtained using eq 2 was 0.99823 (Figure 5e). The limit of detection (LOD) was determined to be 0.5 μM (0.163 ppm) using eq 3.

Photoinduced electron transfer (PET) between Pery-DHTP-BZ-COP and Pb²⁺ ions is a potential mechanism underlying the sensor's detection ability. Zeta-potential analysis was performed to investigate this electron transfer process (Figure S7a,b and Table S1). The zeta-potential of Pery-DHTP-BZ-COP shifted from −32.06 to +22.04 mV upon the introduction of Pb²⁺ ions, indicating a strong interaction between the Pery-DHTP-BZ-COP and Pb²⁺ ions. This shift suggests that Pb²⁺ ions attach to the surface of Pery-DHTP-BZ-COP, altering the surface charge and potentially facilitating electron movement. When excited, electrons can transfer from Pery-DHTP-BZ-COP to Pb²⁺ ions, which are strong acceptors, resulting in fluorescence quenching. The zeta-potential change supports the PET process by indicating significant adsorption or complex formation between Pb²⁺ ions and Pery-DHTP-BZ-COP. The shift from negative to positive zeta-potential implies that Pb²⁺ ions are neutralizing or overcompensating for the original charge of the Pery-DHTP-BZ-COP. Other metal ions

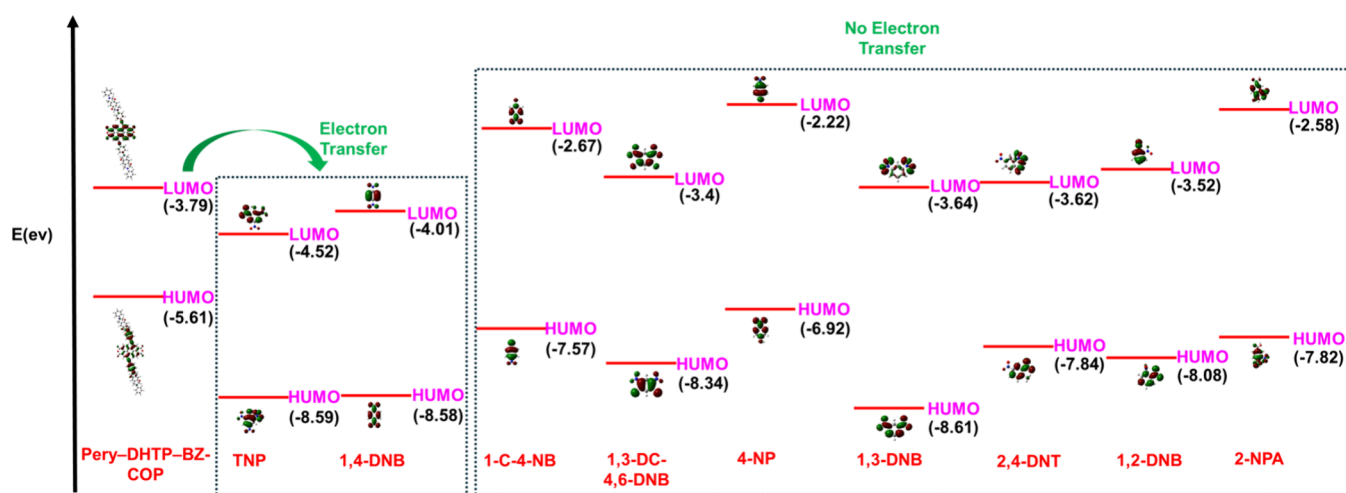


Figure 7. Fluorescence quenching mechanism of Pery-DHTP-BZ-COP by the TNP material.

do not participate effectively in the PET mechanism with Pery-DHTP-BZ-COP, as they do not quench fluorescence. These metal ions may lack the necessary electrical properties or fail to form the required complexes for electron transfer from the excited polymer, even if they can alter the zeta-potential. Although the zeta-potential values indicate that other metal ions interact with Pery-DHTP-BZ-COP, these interactions do not establish a suitable pathway for electron transfer. Nitroaromatic compounds are hazardous pollutants posing a severe threat to human health and the environment. Given the superior fluorescence properties and electron-rich benzene backbone of Pery-DHTP-BZ-COP, we investigated its potential for detecting electron-deficient nitroaromatic compounds using a fluorescence quenching approach. Solutions of various nitroaromatic compounds (Scheme S4) were prepared in THF and then added to Pery-DHTP-BZ-COP dispersed in methanol. The fluorescence quenching behavior was monitored under UV light and through PL spectroscopy at room temperature (Figure 6). Figure 6a compares the effects of different nitroaromatic compounds on the fluorescence of Pery-DHTP-BZ-COP under UV light. The bright yellow emission of the COP exhibited a significant quenching response upon the introduction of trinitrophenol (TNP), visually indicating its detection potential for this specific compound. PL spectra in Figure 6b support this observation, showing a substantial decrease in fluorescence intensity for TNP compared to those of other nitroaromatic compounds. These findings demonstrate a remarkable selectivity of Pery-DHTP-BZ-COP for TNP detection. The fluorescence quenching efficiency for TNP was calculated to be 99% (Figure 6c), significantly higher than that for any other tested nitroaromatic compound. To quantify the sensor's sensitivity toward TNP, a fluorescence titration experiment was conducted (Figure 6d). The TNP concentration was varied from 0 to 30 μM , and the fluorescence intensity displayed a linear decrease with increasing concentration. The linear correlation coefficient was determined to be 0.99769 (Figure 6e). The LOD value of Pery-DHTP-BZ-COP for the TNP was calculated to be 0.7 μM (0.16 ppm). Table S2 compares the limit of detection (LOD) of Pery-DHTP-BZ-COP for TNP with those of other porous materials. To understand the exceptionally high sensitivity and selectivity of Pery-DHTP-BZ-COP toward TNP, we investigated the fluorescence quenching mechanism.

Since nitroaromatic compounds are electron-deficient, fluorescence quenching likely occurs through photoinduced electron transfer (PET). The efficiency of PET depends on the energy levels of the highest occupied molecular orbital (HOMO) and the lowest unoccupied molecular orbital (LUMO) for both the donor (Pery-DHTP-BZ-COP) and the acceptor (nitroaromatic compound). Efficient electron transfer from the COP to the analyte (quenching) occurs when the donor's LUMO level is higher in energy than the acceptor's LUMO level. Using density functional theory (DFT) calculations, we determined the HOMO and LUMO energy levels for Pery-DHTP-BZ-COP and various nitroaromatic compounds. In Figure 7, the LUMO level of Pery-DHTP-BZ-COP (-3.79 eV) lies at a higher energy level compared to that of TNP (-4.52 eV) and 1,4-DNP (-4.01 eV). In contrast, the LUMO level of Pery-DHTP-BZ-COP is lower than those of other nitroaromatic compounds.

This energy level alignment facilitates efficient electron transfer to the TNP and 1,4-DNP, leading to fluorescence quenching. For other nitroaromatic compounds, electron transfer is less favorable, explaining the observed selectivity. To corroborate the PET mechanism, we employed zeta-potential measurements to investigate electron transfer between Pery-DHTP-BZ-COP and TNP (Figure S7a,c). The zeta-potential of Pery-DHTP-BZ-COP shifted from -32.04 to $+24.58$ mV upon the introduction of TNP. This decrease suggests a reduction in electrostatic repulsion, which can facilitate electron transfer from the COP to TNP, further supporting the PET-based quenching mechanism. The combined evidence from energy level calculations and zeta-potential measurements strongly suggests that PET plays a crucial role in the exceptional sensitivity and selectivity of Pery-DHTP-BZ-COP for TNP detection. This understanding paves the way for the development of even more sophisticated fluorescent sensors for targeted nitroaromatic explosives detection. The FTIR spectra (Figure S8) of Pery-DHTP-BZ-COP, Pery-DHTP-BZ-COP@Pb²⁺, and Pery-DHTP-BZ-COP@TNP after the sensing process revealed consistent absorption peaks at 3053, 2175, 1750, 1602, and 927 cm^{-1} . These peaks correspond to aromatic C–H, C \equiv C, C=O, C=C, and the oxazine ring, respectively, demonstrating the chemical stability of Pery-DHTP-BZ-COP.

CONCLUSION

This study describes the successful synthesis of a fluorescent material, Pery-DHTP-BZ-COP, using the Sonogashira–Hagihara coupling reaction. The resulting material displayed excellent thermal stability (char yield of 57 wt %) and fluorescence properties. We further explored the potential of Pery-DHTP-BZ-COP as a fluorescent probe for selective and sensitive detection of Pb^{2+} ions and TNP, a type of nitroaromatic explosive. The fluorescence quenching observed in Pery-DHTP-BZ-COP upon exposure to TNP and Pb^{2+} ions is attributed to PET. This research paves the way for real-time applications of functional porous materials like Pery-DHTP-BZ-COP in sensing TNP and Pb^{2+} ions. The findings hold promise for the development of even more effective materials with enhanced selectivity and sensitivity for ion detection.

ASSOCIATED CONTENT

Supporting Information

The Supporting Information is available free of charge at <https://pubs.acs.org/doi/10.1021/acscapm.4c01514>.

Additional experimental details, materials, and methods, including synthesis, and characterizations of FTIR spectrum of Pery-Br₂, XRD profile of Pery-DHTP-BZ-COP, and photophysical measurements of dispersed Pery-DHTP-BZ-COP in MeOH/H₂O mixtures, different pH and different metal ions and zeta potential of Pery-DHTP-BZ-COP, Pery-DHTP-BZ-COP@ Pb^{2+} , and Pery-DHTP-BZ-COP@TNP and comparison of LOD of Pery-DHTP-BZ-COP for TNP with other porous materials (PDF)

AUTHOR INFORMATION

Corresponding Author

Shiao-Wei Kuo – Department of Materials and Optoelectronic Science, Center for Functional Polymers and Supramolecular Materials, National Sun Yat-Sen University, Kaohsiung 804, Taiwan; Department of Medicinal and Applied Chemistry, Kaohsiung Medical University, Kaohsiung 807, Taiwan;
✉ orcid.org/0000-0002-4306-7171; Email: kuosw@faculty.nsysu.edu.tw

Authors

Mohsin Ejaz – Department of Materials and Optoelectronic Science, Center for Functional Polymers and Supramolecular Materials, National Sun Yat-Sen University, Kaohsiung 804, Taiwan

Mohamed Gamal Mohamed – Department of Materials and Optoelectronic Science, Center for Functional Polymers and Supramolecular Materials, National Sun Yat-Sen University, Kaohsiung 804, Taiwan; Department of Chemistry, Faculty of Science, Assiut University, Assiut 71516, Egypt;
✉ orcid.org/0000-0003-0301-8372

Complete contact information is available at:
<https://pubs.acs.org/doi/10.1021/acscapm.4c01514>

Notes

The authors declare no competing financial interest.

ACKNOWLEDGMENTS

This study was supported financially by the National Science and Technology Council, Taiwan, under Contracts NSTC 113-2221-E-110-012-MY3 and 113-2221-E-110-001. The

authors thank the staff at National Sun Yat-sen University for their assistance with the TEM (ID: EM022600) experiments.

REFERENCES

- (1) Coke, K.; Johnson, M. J.; Robinson, J. B.; Rettie, A. J. E.; Miller, T. S.; Shearing, P. R. Illuminating Polysulfide Distribution in Lithium Sulfur Batteries; Tracking Polysulfide Shuttle Using Operando Optical Fluorescence Microscopy. *ACS Appl. Mater. Interfaces* **2024**, *16*, 20329–20340.
- (2) Saleh, T. A.; Mustaqeem, M.; Khaled, M. Water treatment technologies in removing heavy metal ions from wastewater: A review. *Environ. Nanotechnol. Monit. Manage.* **2022**, *17*, No. 100617.
- (3) Ding, Q.; Li, C.; Wang, H.; Xu, C.; Kuang, H. Electrochemical detection of heavy metal ions in water. *Chem. Commun.* **2021**, *57*, 7215–7231.
- (4) Chen, Z.; Zhang, Z.; Qi, J.; You, J.; Ma, J.; Chen, L. Colorimetric detection of heavy metal ions with various chromogenic materials: Strategies and applications. *J. Hazard. Mater.* **2023**, *441*, No. 129889.
- (5) Unnikrishnan, B.; Lien, C.-W.; Chu, H.-W.; Huang, C.-C. A review on metal nanozyme-based sensing of heavy metal ions: Challenges and future perspectives. *J. Hazard. Mater.* **2021**, *401*, No. 123397.
- (6) Celik, A.; Baker, D. R.; Arslan, Z.; Zhu, X.; Blanton, A.; Nie, J.; Yang, S.; Ma, S.; Han, F. X.; Islam, S. M. Highly efficient, rapid, and concurrent removal of toxic heavy metals by the novel 2D hybrid LDH-[Sn₂S₆]. *Chem. Eng. J.* **2021**, *426*, No. 131696.
- (7) Feng, X.; Long, R.; Wang, L.; Liu, C.; Bai, Z.; Liu, X. A review on heavy metal ions adsorption from water by layered double hydroxide and its composites. *Sep. Purif. Technol.* **2022**, *284*, No. 120099.
- (8) Gao, X.; Guo, C.; Hao, J.; Zhao, Z.; Long, H.; Li, M. Adsorption of heavy metal ions by sodium alginate based adsorbent—a review and new perspectives. *Int. J. Biol. Macromol.* **2020**, *164*, 4423–4434.
- (9) Oghenerobor Benjamin, A.; Gladys Onolunose, O.; Tomilola Debby, O. Heavy Metal Pollutants in Wastewater Effluents: Sources, Effects and Remediation. *Adv. Biosci. Biotechnol.* **2014**, *2*, 37–43.
- (10) Zaynab, M.; Al-Yahyai, R.; Ameen, A.; Sharif, Y.; Ali, L.; Fatima, M.; Khan, K. A.; Li, S. Health and environmental effects of heavy metals. *J. King Saud. Univ. Sci.* **2022**, *34* (1), No. 101653.
- (11) Mitra, S.; Chakraborty, A. J.; Tareq, A. M.; Emran, T. B.; Nainu, F.; Khusro, A.; Idris, A. M.; Khandaker, M. U.; Osman, H.; Alhumaydhi, F. A.; Simal-Gandara, J. Impact of heavy metals on the environment and human health: Novel therapeutic insights to counter the toxicity. *J. King Saud Univ. Sci.* **2022**, *34*, No. 101865.
- (12) Singh, H.; Bamrah, A.; Bhardwaj, S. K.; Deep, A.; Khatri, M.; Kim, K.-H.; Bhardwaj, N. Nanomaterial-based fluorescent sensors for the detection of lead ions. *J. Hazard. Mater.* **2021**, *407*, No. 124379.
- (13) Tahir, M. B.; Arif, S.; Sagir, M.; Batoool, A. Semiconductor-Based Photocatalytic Nanomaterials for Environmental Applications. In *Encyclopedia of Renewable and Sustainable Materials*; Hashmi, S., Choudhury, I. A., Eds.; Elsevier: 2020; pp 320–325.
- (14) Shi, L.; Wang, N.; Hu, X.; Yin, D.; Wu, C.; Liang, H.; Cao, W.; Cao, H. Acute toxic effects of lead (Pb^{2+}) exposure to rare minnow (*Gobiocypris rarus*) revealed by histopathological examination and transcriptome analysis. *Environ. Toxicol. Pharmacol.* **2020**, *78*, No. 103385.
- (15) Virgolini, M. B.; Aschner, M. Molecular mechanisms of lead neurotoxicity. *Adv. Neurotoxicol.* **2021**, *5*, 159–213.
- (16) Bilal, M.; Bagheri, A. R.; Bhatt, P.; Chen, S. Environmental occurrence, toxicity concerns, and remediation of recalcitrant nitroaromatic compounds. *J. Environ. Manage.* **2021**, *291*, No. 112685.
- (17) Verbitskiy, E. V.; Rusinov, G. L.; Chupakhin, O. N.; Charushin, V. N. Design of fluorescent sensors based on azaheterocyclic push-pull systems towards nitroaromatic explosives and related compounds: A review. *Dyes Pigm.* **2020**, *180*, No. 108414.
- (18) Taya, P.; Maiti, B.; Kumar, V.; De, P.; Satapathi, S. Design of a novel FRET based fluorescent chemosensor and their application for

highly sensitive detection of nitroaromatics. *Sens. Actuators, B* **2018**, *255*, 2628–2634.

(19) Chongdar, S.; Mondal, U.; Chakraborty, T.; Banerjee, P.; Bhaumik, A. A Ni-MOF as Fluorescent/Electrochemical Dual Probe for Ultrasensitive Detection of Picric Acid from Aqueous Media. *ACS Appl. Mater. Interfaces* **2023**, *15*, 14575–14586.

(20) Qiu, Z.-J.; Fan, S.-T.; Xing, C.-Y.; Song, M.-M.; Nie, Z.-J.; Xu, L.; Zhang, S.-X.; Wang, L.; Zhang, S.; Li, B.-J. Facile Fabrication of an AIE-Active Metal–Organic Framework for Sensitive Detection of Explosives in Liquid and Solid Phases. *ACS Appl. Mater. Interfaces* **2020**, *12*, 55299–55307.

(21) Zhang, C.; Sun, F.; He, Y. Porous Organic Frameworks Constructed by the Synergetic Effect of Covalent Bonds and Hydrogen Bonds for the Selective Identification and Detection of Explosives. *ACS Appl. Mater. Interfaces* **2023**, *15*, 9970–9977.

(22) Guo, X.; Gao, B.; Cui, X.; Wang, J.; Dong, W.; Duan, Q.; Fei, T.; Su, Z. PL sensor for sensitive and selective detection of 2,4,6-trinitrophenol based on carbazole and tetraphenylsilane polymer. *Dyes Pigm.* **2021**, *191*, No. 109379.

(23) Zhu, H.; Geng, T.-M.; Tang, K.-B. Fully Flexible Covalent Organic Frameworks for Fluorescence Sensing 2,4,6-Trinitrophenol and p-Nitrophenol. *Polymers* **2023**, *15*, 653.

(24) Khan, I.; Shah, T.; Tariq, M. R.; Ahmad, M.; Zhang, B. Understanding the Toxicity of Trinitrophenol and Promising Decontamination Strategies for its Neutralization: Challenges and Future Perspectives. *J. Environ. Chem. Eng.* **2024**, *12*, No. 112720.

(25) Preethi, P. S.; Hariharan, N. M.; Kumar, S. D.; Rameshpathy, M.; Subbaiya, R.; Karmegam, N. Actinobacterial peroxidase-mediated biodeterioration of hazardous explosive, 2, 4, 6, trinitrophenol by in silico and in vitro approaches. *Environ. Geochem. Health* **2024**, *46*, 102.

(26) Liu, X.; Han, Y.; Wang, G.; Wang, Y.; Chen, J.; Shu, Y.; Wang, J.-H.; Qiu, H. Kadsura-Shaped Covalent–Organic Framework Nanostructures for the Sensitive Detection and Removal of 2,4,6-Trinitrophenol. *ACS Appl. Nano Mater.* **2022**, *5*, 6422–6429.

(27) Mahto, M. K.; Samanta, D.; Shaw, M.; Shaik, M. A. S.; Basu, R.; Mondal, I.; Bhattacharya, A.; Pathak, A. Blue-Emissive Nitrogen-Doped Carbon Dots for Picric Acid Detection: Molecular Fluorescence Quenching Mechanism. *ACS Appl. Nano Mater.* **2023**, *6*, 8059–8070.

(28) Koç, Ö. K.; Üzer, A.; Apak, R. Heteroatom-Doped Carbon Quantum Dots and Polymer Composite as Dual-Mode Nanoprobe for Fluorometric and Colorimetric Determination of Picric Acid. *ACS Appl. Mater. Interfaces* **2023**, *15*, 42066–42079.

(29) Wang, X.; Zhang, X.; Cao, H.; Huang, Y. A facile and rapid approach to synthesize uric acid-capped Ti₃C₂ MXene quantum dots for the sensitive determination of 2,4,6-trinitrophenol both on surfaces and in solution. *J. Mater. Chem. B* **2020**, *8*, 10837–10844.

(30) Mohamed, M. G.; El-Mahdy, A. F. M.; Kotp, M. G.; Kuo, S.-W. Advances in porous organic polymers: syntheses, structures, and diverse applications. *Mater. Adv.* **2022**, *3*, 707–733.

(31) Ejaz, M.; Mohamed, M. G.; Huang, W.-C.; Kuo, S.-W. Pyrene-based covalent organic polymers with nano carbonaceous composites for efficient supercapacitive energy storage. *J. Mater. Chem. A* **2023**, *11*, 22868–22883.

(32) Samy, M. M.; Mohamed, M. G.; El-Mahdy, A. F. M.; Mansoure, T. H.; Wu, K. C. W.; Kuo, S.-W. High-Performance Supercapacitor Electrodes Prepared From Dispersions of Tetrabenzonaphthalene-Based Conjugated Microporous Polymers and Carbon Nanotubes. *ACS Appl. Mater. Interfaces* **2021**, *13*, 51906–51916.

(33) Mohamed, M. G.; Chaganti, S. V.; Sharma, S. U.; Samy, M. M.; Ejaz, M.; Lee, J.-T.; Zhang, K.; Kuo, S.-W. Constructing Conjugated Microporous Polymers Containing the Pyrene-4,5,9,10-Tetraone Unit for Energy Storage. *ACS Appl. Energy Mater.* **2022**, *5*, 10130–10140.

(34) Singh, P. N.; Mohamed, M. G.; Chaganti, S. V.; Sharma, S. U.; Ejaz, M.; Lee, J.-T.; Kuo, S.-W. Rational Design of Ultrastable Conjugated Microporous Polymers Based on Pyrene and Perylene Units as High-Performance Organic Electrode Materials for Supercapacitor Applications. *ACS Appl. Energy Mater.* **2023**, *6*, 8277–8287.

(35) Zhang, Y.; Hong, X.; Cao, X.-M.; Huang, X.-Q.; Hu, B.; Ding, S.-Y.; Lin, H. Functional Porous Organic Polymers with Conjugated Triaryl Triazine as the Core for Superfast Adsorption Removal of Organic Dyes. *ACS Appl. Mater. Interfaces* **2021**, *13*, 6359–6366.

(36) Giri, A.; Biswas, S.; Hussain, M. D. W.; Dutta, T. K.; Patra, A. Nanostructured Hypercrosslinked Porous Organic Polymers: Morphological Evolution and Rapid Separation of Polar Organic Micropollutants. *ACS Appl. Mater. Interfaces* **2022**, *14*, 7369–7381.

(37) Mow, R. E.; Russell-Parks, G. A.; Redwine, G. E. B.; Petel, B. E.; Gennett, T.; Braunecker, W. A. Polymer-Coated Covalent Organic Frameworks as Porous Liquids for Gas Storage. *Chem. Mater.* **2024**, *36*, 1579–1590.

(38) Mousa, A. O.; Lin, Z.-I.; Chaganti, S. V.; Chuang, C.-H.; Chen, C.-K.; Kuo, S.-W.; Mohamed, M. G. Bifunctional imidazolium linked tetraphenylethene based conjugated microporous polymers for dynamic antibacterial properties and supercapacitor electrodes. *Polym. Chem.* **2024**, *15*, 397–411.

(39) Zhang, Z.; Jia, J.; Zhi, Y.; Ma, S.; Liu, X. Porous organic polymers for light-driven organic transformations. *Chem. Soc. Rev.* **2022**, *51*, 2444–2490.

(40) Singh, N.; Son, S.; An, J.; Kim, I.; Choi, M.; Kong, N.; Tao, W.; Kim, J. S. Nanoscale porous organic polymers for drug delivery and advanced cancer theranostics. *Chem. Soc. Rev.* **2021**, *50*, 12883–12896.

(41) Mohamed, M. G.; Elsayed, M. H.; Li, C.-J.; Hassan, A. E.; Mekhemer, I. M. A.; Musa, A. F.; Hussien, M. K.; Chen, L.-C.; Chen, K.-H.; Chou, H.-H.; Kuo, S. W. Reticular design and alkyne bridge engineering in donor– π –acceptor type conjugated microporous polymers for boosting photocatalytic hydrogen evolution. *J. Mater. Chem. A* **2024**, *12*, 7693–7710.

(42) Sharma, S. U.; Elsayed, M. H.; Mekhemer, I. M. A.; Meng, T. S.; Chou, H.-H.; Kuo, S.-W.; Mohamed, M. G. Rational design of pyrene and thienyltriazine-based conjugated microporous polymers for high-performance energy storage and visible-light photocatalytic hydrogen evolution from water. *Giant* **2024**, *17*, No. 100217.

(43) Wang, S.; Li, H.; Huang, H.; Cao, X.; Chen, X.; Cao, D. Porous organic polymers as a platform for sensing applications. *Chem. Soc. Rev.* **2022**, *51*, 2031–2080.

(44) Tan, K. T.; Ghosh, S.; Wang, Z.; Wen, F.; Rodriguez-Sanmiguel, D.; Feng, J.; Huang, N.; Wang, W.; Zamora, F.; Feng, X.; Thomas, A.; Jiang, D. Covalent organic frameworks. *Nat. Rev. Methods Primers* **2023**, *3*, 1.

(45) Mousa, A. O.; Mohamed, M. G.; Lin, Z.-I.; Chuang, C.-H.; Chen, C.-K.; Kuo, S.-W. Construction of cationic conjugated microporous polymers containing pyrene units through post-cationic modification for enhanced antibacterial performance. *J. Taiwan Inst. Chem. Eng.* **2024**, *157*, No. 105448.

(46) Zhu, H.; Qin, Y.; Guo, Y.; Shen, Z.; Imran, M.; Asim Mushtaq, M.; Zhang, Z.; Ni, C.; Chen, Y.; Ding, Y.; Gul, H.; Zou, J.; Tsiakaras, P.; Hsu, H.-Y.; Zhao, J. Covalent organic polymers for efficient removal of iodine from gas- and liquid-phase environments. *Chem. Eng. J.* **2024**, *484*, No. 149739.

(47) Xiong, J.-B.; Ban, D.-D.; Zhou, Y.-J.; Du, H.-J.; Zhao, A.-W.; Xie, L.-G.; Liu, G.-Q.; Chen, S.-R.; Mi, L.-W. Fluorescent porous organic polymers for detection and adsorption of nitroaromatic compounds. *Sci. Rep.* **2022**, *12*, 15876.

(48) Said, A. I.; Gamal Mohamed, M. G.; Madhu, M.; Singh, P. N.; Chaganti, S. V.; Elsayed, M. H.; Tseng, W. L.; Raymo, F. M.; Kuo, S.-W. Bifunctional luminescent conjugated microporous polymers containing BODIPY and tetraphenylethene units for highly efficient energy storage and enhanced sensing of Cu²⁺ ions. *Polymer* **2024**, *300*, No. 126988.

(49) Mohamed, M. G.; Hu, H.-Y.; Santhoshkumar, S.; Madhu, M.; Mansoure, T. H.; Hsiao, C.-W.; Ye, Y.; Huang, C.-W.; Tseng, W.-L.; Kuo, S.-W. Design and synthesis of bifunctional conjugated microporous polymers containing tetraphenylethene and bisulfone units for energy storage and fluorescent sensing of p-nitrophenol. *Colloids Surf. A: Physicochem. Eng. Asp.* **2024**, *680*, No. 132675.

- (50) Mohamed, M. G.; Chen, C.-C.; Zhang, K.; Kuo, S.-W. Construction of three-dimensional porous organic polymers with enhanced CO₂ uptake performance via solid-state thermal conversion from tetrahedral benzoxazine-linked precursor. *Eur. Polym. J.* **2023**, *200*, No. 112551.
- (51) Ejaz, M.; Mohamed, M. G.; Kuo, S.-W. Solid state chemical transformation provides a fully benzoxazine-linked porous organic polymer displaying enhanced CO₂ capture and supercapacitor performance. *Polym. Chem.* **2023**, *14*, 2494–2509.
- (52) Ejaz, M.; Mohamed, M. G.; Chen, Y.-T.; Zhang, K.; Kuo, S.-W. Porous carbon materials augmented with heteroatoms derived from hyperbranched biobased benzoxazine resins for enhanced CO₂ adsorption and exceptional supercapacitor performance. *J. Energy Storage* **2024**, *78*, No. 110166.
- (53) Mohamed, M. G.; Li, C.-J.; Khan, M. A. R.; Liaw, C.-C.; Zhang, K.; Kuo, S.-W. Formaldehyde-Free Synthesis of Fully Bio-Based Multifunctional Bisbenzoxazine Resins from Natural Renewable Starting Materials. *Macromolecules* **2022**, *55*, 3106–3115.
- (54) Mohamed, M. G.; Chang, W.-C.; Kuo, S.-W. Crown Ether- and Benzoxazine-Linked Porous Organic Polymers Displaying Enhanced Metal Ion and CO₂ Capture through Solid-State Chemical Transformation. *Macromolecules* **2022**, *55*, 7879–7892.
- (55) Lu, Y.; Liu, J.; Zhao, W.; Zhang, K. Bio-benzoxazine structural design strategy toward highly thermally stable and intrinsically flame-retardant thermosets. *Chem. Eng. J.* **2023**, *457*, No. 141232.
- (56) Sahu, S.; Niranjana, R.; Priyadarshini, R.; Lochab, B. Benzoxazine-grafted-chitosan biopolymer films with inherent disulfide linkage: Antimicrobial properties. *Chemosphere* **2023**, *328*, No. 138587.
- (57) Sha, X.-L.; Fei, P.; Shen, B.; Chen, J.; Liu, Z.; Sun, Y.; Miao, J.-T. Solvent-free Synthesis of Alkynyl-Based Biobased Benzoxazine Resins with Excellent Heat Resistance. *ACS Appl. Polym. Mater.* **2023**, *5*, 3015–3022.
- (58) Liu, Y.-L.; Chang, C.-Y.; Hsu, C.-Y.; Tseng, M.-C.; Chou, C.-I. Preparation, characterization, and properties of fluorene-containing benzoxazine and its corresponding cross-linked polymer. *J. Polym. Sci., Part A: Polym. Chem.* **2010**, *48*, 4020–4026.
- (59) Fang, B.; Lu, X.; Hu, J.; Zhang, G.; Zheng, X.; He, L.; Cao, J.; Gu, J.; Cao, F. pH controlled green luminescent carbon dots derived from benzoxazine monomers for the fluorescence turn-on and turn-off detection. *J. Colloid Interface Sci.* **2019**, *536*, 516–525.
- (60) Lin, R.-C.; Kuo, S.-W. Well-defined benzoxazine/triphenylamine-based hyperbranched polymers with controlled degree of branching. *RSC Adv.* **2018**, *8*, 13592–13611.
- (61) Goto, M.; Yajima, T.; Minami, M.; Sogawa, H.; Sanda, F. Synthesis and Cross-Linking of a Benzoxazine-Containing Anthracene Moiety: Thermally Stable Photoluminescent Benzoxazine Resin. *Macromolecules* **2020**, *53*, 6640–6648.
- (62) Su, Y.; Shi, W.; Chen, X.; Zhao, S.; Hui, Y.; Xie, Z. An aggregation-induced emission enhancement fluorescent benzoxazine-derived macromolecule: catalyst-free synthesis and its preliminary application for the determination of aqueous picric acid. *RSC Adv.* **2016**, *6*, 41340–41347.
- (63) Shi, W.; Liu, Q.; Zhang, J.; Zhou, X.; Yang, C.; Zhang, K.; Xie, Z. Tetraphenylethene-decorated functional polybenzoxazines: post-polymerization synthesis via benzoxazine–isocyanide chemistry and application in probing and catalyst fields. *Polym. Chem.* **2019**, *10*, 1130–1139.
- (64) Liu, Y.; Chen, X.; Liu, X.; Guan, W.; Lu, C. Aggregation-induced emission-active micelles: synthesis, characterization, and applications. *Chem. Soc. Rev.* **2023**, *52*, 1456–1490.
- (65) Morimoto, M.; Takagi, Y.; Hioki, K.; Nagasaka, T.; Sotome, H.; Ito, S.; Miyasaka, H.; Irie, M. A turn-on mode fluorescent diarylethene: Solvatochromism of fluorescence. *Dyes Pigm.* **2018**, *153*, 144–149.
- (66) Mohamed, M. G.; Liu, N.-Y.; El-Mahdy, A. F. M.; Kuo, S.-W. Ultrastable luminescent hybrid microporous polymers based on polyhedral oligomeric silsesquioxane for CO₂ uptake and metal ion sensing. *Microporous Mesoporous Mater.* **2021**, *311*, No. 110695.
- (67) Madhu, M.; Santhoshkumar, S.; Hsiao, C. W.; Tseng, W. L.; Kuo, S. W.; Mohamed, M. G. Selective and Sensitive Detection of Fe³⁺ Ions Using a Red-Emissive Fluorescent Probe Based on Triphenylamine and Perylene-Linked Conjugated Microporous Polymer. *Macromol. Rapid Commun.* **2024**, 2400263.
- (68) Aly, K. I.; Sayed, M. M.; Mohamed, M. G.; Kuo, S. W.; Younis, O. A facile synthetic route and dual function of network luminescent porous polyester and copolyester containing porphyrin moiety for metal ions sensor and dyes adsorption. *Microporous Mesoporous Mater.* **2020**, *298*, No. 110063.